OPEN ACCESS



Theory and Transport of Nearly Incompressible Magnetohydrodynamic Turbulence: High Plasma Beta Regime

Abstract

Nearly incompressible magnetohydrodynamic (NI MHD) theory for $\beta \sim 1$ (or $\beta \ll 1$) plasma has been developed and applied to the study of solar wind turbulence. The leading-order term in $\beta \sim 1$ or $\beta \ll 1$ plasma describes the majority of 2D turbulence, while the higher-order term describes the minority of slab turbulence. Here, we develop new NI MHD turbulence transport model equations in the high plasma beta regime. The leading-order term in a $\beta \gg 1$ plasma is fully incompressible and admits both structures (flux ropes or magnetic islands) and slab (Alfvén waves) fluctuations. This paper couples the NI MHD turbulence transport equations with three fluid (proton, electron, and pickup ion) equations, and solves the 1D steady-state equations from 1–75 au. The model is tested against 27 yr of Voyager 2 data, and Ulysses and NH SWAP data. The results agree remarkably well, with some scatter, about the theoretical predictions.

Unified Astronomy Thesaurus concepts: The Sun (1693); Interplanetary turbulence (830); Solar wind (1534); Pickup ions (1239)

1. Introduction

Nearly incompressible (NI) theory was developed originally to explain Kolmogorov-like power spectra (Montgomery et al. 1987) exhibited by interstellar electron density fluctuations (Armstrong et al. 1981, 1995). NI magnetohydrodynamic (MHD) theory was developed largely in the early 1990s for homogeneous flows (Klainerman & Majda 1981, 1982; Montgomery et al. 1987; Zank & Matthaeus 1991, 1992a, 1992b, 1993) and was later extended to inhomogeneous flows (Bhattacharjee et al. 1998; Hunana et al. 2006, 2008; Hunana & Zank 2010). However, NI MHD theory was applied to the study of solar wind turbulence for the first time in the late 2010s by Zank et al. (2017). Besides the application of inhomogeneous NI MHD to solar wind turbulence, Zank et al. (2020) developed the spectral theory of NI MHD turbulence for plasma beta $\beta \ll 1$. Zank et al. (2017) tested the NI MHD theory against Helios 2, Ulysses, and Voyager 2 (V2) measurements from the inner heliosphere to the outer heliosphere. Adhikari et al. (2017a) used the NI MHD turbulence model to study solar wind heating from 1–75 au. Similarly, Zank et al. (2018a) investigated the heating of the solar corona by using an NI MHD turbulence transport model. Since then, the NI MHD turbulence model has been applied successfully in the solar atmosphere (Adhikari et al. 2020a, 2022a; Zank et al. 2021, 2022; Telloni et al. 2022b), in the inner heliosphere (Adhikari et al. 2020b, 2021b, 2022c; Telloni et al. 2022a), and in the outer heliosphere (Adhikari

Original content from this work may be used under the terms of the Creative Commons Attribution 4.0 licence. Any further distribution of this work must maintain attribution to the author(s) and the title of the work, journal citation and DOI.

et al. 2017b; Zank et al. 2018b; Nakanotani et al. 2020). In the recent work of Adhikari et al. (2022b), NI MHD theory was used to study the 2D and slab turbulent heating rates in the inner heliosphere. Similarly, NI MHD theory has also been applied to the study of cosmic-ray mean free paths throughout the heliosphere (Zhao et al. 2017, 2018).

Hunana & Zank (2010) developed NI MHD turbulence theory for inhomogeneous flows in different plasma beta regimes $(\beta \gg 1, \beta \ll 1, \text{ and } \beta \sim 1.8$ The formulation of NI MHD turbulence changes with plasma beta regime (Zank & Matthaeus 1993). For a $\beta \gg 1$ plasma, the leading-order incompressible turbulence state is fully 3D, whereas in the $\beta \ll 1$ or $\beta \sim 1$ plasma, the leading-order incompressible turbulence is 2D and the higher-order turbulence is 3D and an admixture of incompressible and compressible fluctuations. In the case of $\beta \gg 1$, the 3D leading-order contribution is fully incompressible and admits both structures (flux ropes or magnetic islands) and slab (Alfvén waves) fluctuations at the same order. By contrast, when $\beta \lesssim 1$, the leading-order turbulence is 2D in the plane orthogonal to the strong mean magnetic field and therefore comprises structures only. The higher-order correction describes a minority incompressible slab (Alfvénic) component and a compressible magnetosonic

Using the induction and momentum equations corresponding to $\beta \sim 1$ plasma from Hunana & Zank (2010), Zank et al. (2017) derived the NI MHD 2D+slab turbulence transport

 $[\]overline{^8}$ The plasma beta β is the ratio between the thermal plasma pressure and the magnetic pressure. In the inner heliosphere, $\beta \leqslant 1$. However, in the outer heliosphere due to the presence of pickup ions (PUIs; Kallenbach et al. 2000; Cannon et al. 2014; Aggarwal et al. 2016; Fisher et al. 2016; Pine et al. 2020), β may increase to become larger than 1.

model equations. The 2D turbulence transport equations do not include the Alfvén velocity, whereas the slab turbulence transport equations include the Alfvén velocity (see also Wang et al. 2022, for the $\beta \ll 1$ plasma). In contrast, the 3D incompressible MHD two-component model developed by Oughton et al. (2011) in the high plasma beta regime includes the Alfvén velocity in both the 2D and slab turbulence transport equations.

Following Hunana & Zank (2010), we develop the NI MHD turbulence transport equations in the high plasma beta regime $(\beta \gg 1)$. These describe the radial evolution of outward and inward Elsässer energies and the corresponding correlation lengths, and the residual energy and the corresponding correlation length. We couple the NI MHD turbulence transport model equations with a three fluid (proton, electron, and PUI) solar wind model (e.g., Zank et al. 2018b; Adhikari et al. 2021b), and solve the coupled equations from 1–75 au. The theoretical results of the turbulence energies and the correlation lengths are validated against 27 yr of Voyager 2 (V2) measurements. The theoretical results for the solar wind parameters are validated against V2 measurements, 2 yr (1995–1997) of near-ecliptic Ulysses measurements, and 13 yr (2008-2021) of New Horizons Solar Wind Around Pluto (NH SWAP; McComas et al. 2008, 2021, 2022) measurements. Similarly, the theoretical results for the PUI parameters are compared against NH SWAP measurements.

This manuscript is structured as follows. Section 2 discusses the NI MHD turbulence transport equations. Section 3 presents the 1D steady-state NI MHD turbulence transport model equations. Section 4 discusses the transport equation of density fluctuations. Section 5 discusses the three fluid solar wind model. Sections 6 and 7 discuss the radial evolution of turbulence and background solar wind from 1–75 au, respectively. Finally, Section 8 provides our conclusions.

2. Transport of NI MHD Turbulence in an Inhomogeneous $\beta \gg 1$ Plasma

NI MHD theory has been extensively described elsewhere (Zank & Matthaeus 1991, 1992a, 1992b, 1993; Hunana & Zank 2010; Zank et al. 2017). To derive the NI MHD turbulence transport equations, we start from the normalized induction and momentum equations (Hunana & Zank 2010),

$$\frac{\partial \mathbf{B}'}{\partial t} + (\mathbf{U}_{sw} + \mathbf{u}') \cdot \nabla \mathbf{B}' - (\mathbf{B}_{sw} + \mathbf{B}') \cdot \nabla \mathbf{u}' + (\mathbf{B}_{sw} + \mathbf{B}') \nabla \cdot \mathbf{u}'
= \chi \mathbf{B}' \cdot \nabla \mathbf{U}_{sw} - \chi \mathbf{u}' \cdot \nabla \mathbf{B}_{sw} - \chi \mathbf{B}' \nabla \cdot \mathbf{U}_{sw};$$
(1)
$$(\rho_{sw} + \rho') \frac{\partial \mathbf{u}'}{\partial t} + (\rho_{sw} + \rho') \mathbf{U}_{sw} \cdot \nabla \mathbf{u}' + (\rho_{sw} + \rho') \mathbf{u}' \cdot \nabla \mathbf{u}'
+ \chi (\rho_{sw} + \rho') \mathbf{u}' \cdot \nabla \mathbf{U}_{sw} + \chi \rho' \mathbf{U}_{sw} \cdot \nabla \mathbf{U}_{sw}
= -\frac{1}{\epsilon^{2}} \nabla P' + (\nabla \times \mathbf{B}') \times \mathbf{B}_{sw} + (\nabla \times \mathbf{B}') \times \mathbf{B}'
+ \chi (\nabla \times \mathbf{B}_{sw}) \times \mathbf{B}',$$
(2)

where B' is the fluctuating magnetic field, u' is the fluctuating solar wind speed, $U_{\rm sw}$ is the background solar wind speed, $B_{\rm sw}$ is the background magnetic field, $\rho_{\rm sw}$ is the background solar wind density, ρ' is the fluctuating solar wind density, and $\chi = L/R$ where L is a characteristic length scale of the fluctuations and R is a characteristic scale measuring the

variation in the inhomogeneity of the background parameters. The parameter $\epsilon(\equiv M_{s0} \ll 1)$ is a small dimensionless quantity. $M_{s0}(=\langle u^2\rangle^{1/2}/C_s)$ is the turbulent Mach number, where $\langle u^2\rangle$ is the turbulent kinetic energy and C_s is the speed of sound. We use the ansatz (Hunana & Zank 2010)

$$\mathbf{u}' = \mathbf{u}^{\infty} + \epsilon \mathbf{u}^{*}; \ P' = \epsilon^{2} (P^{\infty} + P^{*});$$
$$\rho' = \epsilon \rho^{\infty} + \epsilon^{2} \rho^{*}; \ \mathbf{B}' = \mathbf{B}^{\infty} + \epsilon \mathbf{B}^{*}, \tag{3}$$

in Equations (1) and (2) and renormalize $P^{\infty} = \epsilon^2 P^{\infty}$, $P^* = \epsilon^2 P^*$, and $P^$

$$\rho_{\text{sw}} \frac{\partial \boldsymbol{u}^{\infty}}{\partial t} + \rho_{\text{sw}} (\boldsymbol{U}_{\text{sw}} + \boldsymbol{u}^{\infty}) \cdot \nabla \boldsymbol{u}^{\infty} + \rho_{\text{sw}} \boldsymbol{u}^{\infty} \cdot \nabla \boldsymbol{U}_{\text{sw}}$$

$$= -\nabla P^{\infty} + \frac{1}{\mu_{0}} (\nabla \times \boldsymbol{B}^{\infty}) \times \boldsymbol{B}_{\text{sw}}$$

$$+ \frac{1}{\mu_{0}} (\nabla \times \boldsymbol{B}^{\infty}) \times \boldsymbol{B}^{\infty} + \frac{1}{\mu_{0}} (\nabla \times \boldsymbol{B}_{\text{sw}}) \times \boldsymbol{B}^{\infty};$$
(4)

$$\frac{\partial \mathbf{B}^{\infty}}{\partial t} + (\mathbf{U}_{\text{sw}} + \mathbf{u}^{\infty}) \cdot \nabla \mathbf{B}^{\infty} - (\mathbf{B}_{\text{sw}} + \mathbf{B}^{\infty}) \cdot \nabla \mathbf{u}^{\infty}
+ (\mathbf{B}_{\text{sw}} + \mathbf{B}^{\infty}) \nabla \cdot \mathbf{u}^{\infty} = \mathbf{B}^{\infty} \cdot \nabla \mathbf{U}_{\text{sw}} - \mathbf{u}^{\infty} \cdot \nabla \mathbf{B}_{\text{sw}}
- \mathbf{B}^{\infty} \nabla \cdot \mathbf{U}_{\text{sw}};$$
(5)

$$\nabla \cdot \boldsymbol{u}^{\infty} = -\frac{1}{\rho_{\text{sw}}} \boldsymbol{u}^{\infty} \cdot \nabla \rho_{\text{sw}}; \quad \nabla \cdot \boldsymbol{B}^{\infty} = 0, \tag{6}$$

where μ_0 is the magnetic permeability of free space. The leading-order Equations (4)–(6) describe incompressible MHD turbulence, comprising both 2D and slab fluctuations (Zank & Matthaeus 1992a, 1992b, 1993), where 2D and slab fluctuations cannot be distinguished. Therefore, Equations (4)-(6) describe 2D + slab turbulence. This is distinguished from the low and order 1 plasma beta models, i.e., $\beta \ll 1$ and $\beta \sim 1$ plasma, for which the leading-order equations describe 2D turbulence, and the higher-order equations describe slab turbulence (Zank & Matthaeus 1992a, 1992b, 1993; Hunana & Zank 2010; Zank et al. 2017; Wang et al. 2022). Therefore, both leading-order and higher-order equations are required to describe 2D + slab turbulence in the $\beta \ll 1$ and $\beta \sim 1$ plasma. In the large plasma beta case described by Equations (4)–(6), both the 2D and slab contributions are included at the leadingorder, fully incompressible set of equations, which is quite different from the low and order 1 plasma beta equations of Zank et al. (2017). It is also worth noting that in the NI MHD description the fluctuating solar wind speed is not solenoidal $(\nabla \cdot \boldsymbol{u}^{\infty} \neq 0)$, while in the incompressible MHD description, the fluctuating solar wind speed is solenoidal $(\nabla \cdot \mathbf{u} = 0,$ Marsch & Tu 1989; Zhou & Matthaeus 1990a, 1990b).

For simplicity, we remove the superscript " ∞ " from the equation. The leading-order fluctuating Elsässer variables can be defined as

$$z^{\pm} = \boldsymbol{u} \pm \frac{\boldsymbol{B}}{\sqrt{\mu_0 \rho(\boldsymbol{x})}} = \boldsymbol{u} \pm \boldsymbol{v}_{\mathrm{A}},$$

where the background mean density $\rho = \rho(x)$ is assumed to be time stationary and varies as a function of position. The transport Equations (4)-(6) can be written in the Elsässer formulation as

$$\begin{split} &\frac{\partial z^{\pm}}{\partial t} + (\boldsymbol{U}_{\text{sw}} \mp \boldsymbol{V}_{\text{A}}^{\text{sw}}) \cdot \nabla z^{\pm} + z^{\mp} \cdot \nabla z^{\pm} \\ &+ \frac{z^{\pm} - z^{\mp}}{4} \nabla \cdot \boldsymbol{U}_{\text{sw}} + z^{\mp} \cdot \nabla (\boldsymbol{U}_{\text{sw}} \pm \boldsymbol{V}_{\text{A}}^{\text{sw}}) \mp \frac{1}{2} \frac{\boldsymbol{V}_{\text{A}}^{\text{sw}}}{\rho_{\text{sw}}} z^{\pm} \cdot \nabla \rho_{\text{sw}} \\ &- \frac{z^{\pm} - z^{\mp}}{4\rho_{\text{sw}}} z^{\pm} \cdot \nabla \rho_{\text{sw}} \mp \frac{z^{\pm} - z^{\mp}}{4\rho_{\text{sw}}} \boldsymbol{V}_{\text{A}}^{\text{sw}} \cdot \nabla \rho_{\text{sw}} \\ &= -\frac{1}{\rho_{\text{sw}}} \nabla \left(P + \frac{\boldsymbol{B} \cdot \boldsymbol{B}^{\text{sw}}}{\mu_{0}} + \frac{B^{2}}{2\mu_{0}} \right). \end{split}$$
(7)

Equation (7) includes the Alfvén velocity (V_A^{sw}), which confirms that the leading-order transport equation in the $\beta \gg 1$ plasma is fully 3D (Zank & Matthaeus 1992a, 1993). This is the main difference from that in the $\beta \ll 1$ or $\beta \sim 1$ plasma (see Equation (63) of Zank et al. 2017), where the leading-order transport equation of the Elsässer variable does not include the Alfvén velocity, and is 2D. Also, due to the $\nabla \cdot \boldsymbol{u} \neq 0$ in the $\beta \gg 1$ NI MHD theory, Equation (7) is different from that in the incompressible MHD theory (Marsch & Tu 1989; Zhou & Matthaeus 1990a, 1990b).

To derive the turbulence transport equations, we follow the moment hierarchy approach (see Matthaeus et al. 1994; Zank et al. 2012a, 2017). The moments of the Elsässer variables can be written as

$$\langle z^{\pm 2} \rangle = \langle z^{\pm} \cdot z^{\pm} \rangle$$
 and $E_D = \langle z^+ \cdot z^- \rangle$,

where $\langle z^{\pm 2} \rangle$ denotes the outward/inward Elsässer energy, and E_D^{∞} the residual energy. The energy-weighted correlation length corresponding to outward/inward Elsässer energy L^{\pm} and the residual energy L_D can be written as

$$L^{\pm} \equiv \int \langle z^{\pm} \cdot z^{\pm'} \rangle dr \equiv \langle z^{\pm 2} \rangle \lambda^{\pm}$$
 and
 $L_D \equiv \int \langle z^{+} \cdot z^{-'} + z^{+'} \cdot z^{-} \rangle dr \equiv E_D \lambda_D$,

where $z^{\pm \prime}(\equiv z^{\pm}(x+r))$ denotes the lagged Elsässer variable, and λ^{\pm} and λ_D are the correlation lengths corresponding to outward/inward Elsässer energy and the residual energy.

We use the following closures.

1. According to Zank et al. (2012a), the nonlinear term $z^{\mp} \cdot \nabla z^{\pm}$ can be written as

$$NL^{\pm} = z^{\mp} \cdot \nabla z^{\pm} \simeq \alpha z^{\pm} \frac{\langle z^{\mp 2} \rangle^{1/2}}{\lambda^{\pm}},$$

where α is a von Kármán–Taylor constant.

2. The covariance with zero lag can be written as $Q_{ii}(0) = C\delta_{ii}$ (Batchelor 1953). By assuming that turbulence in a plane perpendicular to the mean magnetic field is isotropic (e.g., Zank et al. 2017), we write the following moments (Zank et al. 2012a):

$$\langle (z^{\mp} \cdot \nabla U) \cdot z^{\pm} \rangle = \langle z_{i}^{\mp} z_{j}^{\pm} \rangle \frac{\partial U_{j}}{\partial x_{i}} \delta_{ij}$$

$$= a \langle z^{\pm} \cdot z^{\mp} \rangle \frac{\partial U_{i}}{\partial x_{i}} = a E_{D} \nabla \cdot U;$$

$$\langle (z^{\mp} \cdot \nabla V_{A}) \cdot z^{\pm} \rangle = \langle z_{i}^{\mp} z_{j}^{\pm} \rangle \frac{\partial V_{Aj}}{\partial x_{i}} \delta_{ij}$$

$$= b \langle z^{\pm} \cdot z^{\mp} \rangle \frac{\partial V_{Ai}}{\partial x_{i}} = b E_{D} \nabla \cdot V_{A},$$

where a and b are structural similarity parameters related to the background solar wind speed and Alfvén velocity. We choose a = 1/2 and b = 1/2, yielding the twodimensional form of the mixing tensors (Matthaeus et al. 1994; Zank et al. 2012a).

3. The moment $\langle z^{\pm} \cdot \nabla \rho_{sw} \rangle$ can be written as $\langle z^{\pm} \cdot \nabla \rho_{sw} \rangle \sim \langle z^{\pm 2} \rangle^{1/2} \boldsymbol{n}^{\pm} \cdot \nabla \rho_{sw}$, where \boldsymbol{n}^{\pm} denotes the direction of \boldsymbol{z}^{\pm} . By assuming isotropic turbulence, we approximate $\langle \mathbf{z}^{\pm}\cdot\dot{\nabla}\rho_{\mathrm{sw}}\rangle\sim0.$ This is different from the treatment presented in Zank et al. (2017) in which the leading-order description is 2D.

Using closures (i)–(iii), and the closures (A10) and (C10) from Zank et al. (2012a) (see the Appendix), we derive the following turbulence transport equations:

$$\frac{\partial \langle z^{\pm 2} \rangle}{\partial t} + (U \mp V_{A}) \cdot \nabla \langle z^{\pm 2} \rangle + \left(\frac{1}{2} \nabla \cdot U \pm \nabla \cdot V_{A}\right) \langle z^{\pm 2} \rangle
+ \left(2a - \frac{1}{2}\right) \nabla \cdot U E_{D} \pm (2b - 1) \nabla \cdot V_{A} E_{D}
\mp \frac{b}{\rho} V_{A} \cdot \nabla \rho \langle z^{\pm 2} \rangle = -2\alpha \frac{\langle z^{\pm 2} \rangle \langle z^{\mp 2} \rangle^{1/2}}{\lambda^{\pm}} + 2S^{\pm};$$
(8)

$$\frac{\partial E_{D}}{\partial t} + \boldsymbol{U} \cdot \nabla E_{D} + \frac{1}{2} \nabla \cdot \boldsymbol{U} E_{D} + \left(2a - \frac{1}{2}\right) \nabla \\
\cdot \boldsymbol{U} \frac{\langle z^{+2} \rangle + \langle z^{-2} \rangle}{2} - (2b - 1) \nabla \cdot \boldsymbol{V}_{A} \frac{\langle z^{+2} \rangle - \langle z^{-2} \rangle}{2} \\
+ \frac{1}{2\sqrt{\langle z^{+2} \rangle \langle z^{-2} \rangle}} [\langle z^{+2} \rangle \boldsymbol{V}_{A} \cdot \nabla \langle z^{-2} \rangle - \langle z^{-2} \rangle \boldsymbol{V}_{A} \cdot \nabla \langle z^{+2} \rangle] \\
= -\alpha E_{D} \left(\frac{\langle z^{-2} \rangle^{1/2}}{\lambda^{+}} + \frac{\langle z^{+2} \rangle^{1/2}}{\lambda^{-}}\right) + S_{E_{D}}; \tag{9}$$

$$\frac{\partial \lambda^{\pm}}{\partial t} + (U \mp V_{A}) \cdot \nabla \lambda^{\pm} + \left(a - \frac{1}{4}\right) \nabla \cdot U(\lambda_{D} - 2\lambda^{\pm})
\times \frac{E_{D}}{\langle z^{\pm 2} \rangle} \pm \left(b - \frac{1}{2}\right) \nabla \cdot V_{A}(\lambda_{D} - 2\lambda^{\pm}) \frac{E_{D}}{\langle z^{\pm 2} \rangle}
= 2\beta^{0} \langle z^{\mp 2} \rangle^{1/2} - 2S^{\pm} \frac{\beta^{0}}{\alpha} \frac{\lambda^{\pm}}{\langle z^{\pm 2} \rangle};$$
(10)

(10)

$$\frac{\partial \lambda_{D}}{\partial t} + \boldsymbol{U} \cdot \nabla \lambda_{D} - \left(2a - \frac{1}{2}\right) \frac{\nabla \cdot \boldsymbol{U}}{2E_{D}} [(\lambda_{D} - 2\lambda^{+})\langle z^{+2}\rangle \\
+ (\lambda_{D} - 2\lambda^{-})\langle z^{-2}\rangle] + (2b - 1) \frac{\nabla \cdot \boldsymbol{V}_{A}}{2E_{D}} \\
\times [(\lambda_{D} - 2\lambda^{+})\langle z^{+2}\rangle - (\lambda_{D} - 2\lambda^{-})\langle z^{-2}\rangle] \\
- \left(\frac{\lambda_{D}}{2} - (\lambda^{+}\lambda^{-})^{1/2}\right) \frac{1}{E_{D}} \left[\left(\frac{\langle z^{+2}\rangle}{\langle z^{-2}\rangle}\right)^{1/2} \boldsymbol{V}_{A} \cdot \nabla \langle z^{-2}\rangle \\
- \left(\frac{\langle z^{-2}\rangle}{\langle z^{+2}\rangle}\right)^{1/2} \boldsymbol{V}_{A} \cdot \nabla \langle z^{+2}\rangle\right] + \frac{(\langle z^{+2}\rangle\langle z^{-2}\rangle)^{1/2}}{E_{D}} \\
\times \left[\left(\frac{\lambda^{+}}{\lambda^{-}}\right)^{1/2} \boldsymbol{V}_{A} \cdot \nabla \lambda^{-} - \left(\frac{\lambda^{-}}{\lambda^{+}}\right)^{1/2} \boldsymbol{V}_{A} \cdot \nabla \lambda^{+}\right] \\
= \beta^{0} \lambda_{D} \left(\frac{\langle z^{-2}\rangle^{1/2}}{\lambda^{+}} + \frac{\langle z^{+2}\rangle^{1/2}}{\lambda^{-}}\right) - S_{E_{D}} \frac{\beta^{0}}{\alpha} \frac{\lambda_{D}}{E_{D}}, \tag{11}$$

where β^0 (= $\alpha/2$, Breech et al. 2008) is the von Kármán–Taylor constant. For simplicity, we remove the superscript and subscript "SW" from $V_{\rm A}^{\rm sw}$ and $U_{\rm sw}$. Equations (8) and (10) are the transport equations of the outward/inward Elsässer energy and the corresponding correlation lengths. Equations (9) and (11) are the transport equations of the residual energy and the corresponding correlation length. The parameters S^{\pm} and S_{E_D} denote the sources of turbulence, such as turbulence shear source and PUI source of turbulence. The turbulence shear source is generated due to the difference between the fast and slow solar wind speed, which is important below \sim 5 au. The PUI source of turbulence is generated due to the instability of the ring beam distribution of PUIs in the solar wind plasma. Also, notice that Equations (8)–(11) are derived for $\nabla \cdot \boldsymbol{u} \neq 0$, and are therefore different from the Equations (42)-(46) of Zank et al. (2012a), which were derived by considering $\nabla \cdot \boldsymbol{u} = 0$.

3. 1D Spherically Symmetric Turbulence Model Equations

Assuming $U \gg V_A$ and considering only the super-Alfvénic solar wind (Zank et al. 1996, 2012a,—Appendix D), Equations (8)–(11)can be written in the 1D steady-state form as

$$U\frac{d\langle z^{\pm 2}\rangle}{dr} + \left(\frac{dU}{dr} + \frac{2U}{r}\right) \left[\frac{\langle z^{\pm 2}\rangle}{2} + \left(2a - \frac{1}{2}\right)E_{D}\right]$$

$$= -2\alpha \frac{\langle z^{\pm 2}\rangle \langle z^{\mp 2}\rangle^{1/2}}{\lambda^{\pm}} + 2c^{\pm} \frac{r_{0}|\Delta U|V_{A0}^{2}}{r^{2}}$$

$$+ \frac{f_{D}n_{H}^{\infty}UV'_{A}}{n_{sw}^{0}\tau_{ion}^{0}} \exp\left(\frac{-L}{r}\right); \qquad (12)$$

$$U\frac{dE_{D}}{dr} + \left(\frac{dU}{dr} + \frac{2U}{r}\right) \left(\frac{E_{D}}{2} + \left(2a - \frac{1}{2}\right)\frac{\langle z^{+2}\rangle + \langle z^{-2}\rangle}{2}\right)$$

$$= -\alpha E_{D} \left(\frac{\langle z^{-2}\rangle^{1/2}}{\lambda^{+}} + \frac{\langle z^{+2}\rangle^{1/2}}{\lambda^{-}}\right)$$

$$+ c_{E_{D}} \frac{r_{0}|\Delta U|V_{A0}^{2}}{r^{2}}; \qquad (13)$$

$$U\frac{d\lambda^{\pm}}{dr} + \left(a - \frac{1}{4}\right)\left(\frac{dU}{dr} + \frac{2U}{r}\right)(\lambda_{D} - 2\lambda^{\pm})\frac{E_{D}}{\langle z^{\pm 2}\rangle}$$

$$= 2\beta^{0}\langle z^{\mp 2}\rangle^{1/2} - \frac{\lambda^{\pm}}{\langle z^{\pm 2}\rangle}\frac{\beta^{0}}{\alpha}\left[2c^{\pm}\frac{r_{0}|\Delta U|V_{A0}^{2}}{r^{2}}\right]$$

$$+ \frac{f_{D}n_{\text{sw}}^{m}UV'_{A}}{n_{\text{sw}}^{0}\tau_{\text{ion}}^{0}}\exp\left(\frac{-L}{r}\right); \qquad (14)$$

$$U\frac{d\lambda_{D}}{dr} - \left(2a - \frac{1}{2}\right)\frac{1}{2E_{D}}\left(\frac{dU}{dr} + \frac{2U}{r}\right)$$

$$\times\left[(\lambda_{D} - 2\lambda^{+})\langle z^{+2}\rangle + (\lambda_{D} - 2\lambda^{-})\langle z^{-2}\rangle\right]$$

$$= \beta^{0}\lambda_{D}\left(\frac{\langle z^{-2}\rangle^{1/2}}{\lambda^{+}}\right)$$

$$+ \frac{\langle z^{+2}\rangle^{1/2}}{\lambda^{-}}\right) - c_{E_{D}}\frac{\beta^{0}}{\alpha}\frac{\lambda_{D}}{E_{D}}\frac{r_{0}|\Delta U|V_{A0}^{2}}{r^{2}}. \qquad (15)$$

The von Kármán–Taylor constant α controls the cascade rate of turbulence. Different authors have chosen different values of α to adjust their results. For example, Matthaeus et al. (1999a, 1999b) used $\alpha = 1$, Smith et al. (2006), Breech et al. (2008), and Usmanov et al. (2012) used $\alpha = 0.8$, and Usmanov et al. (2018) used $\alpha = 0.128$. In this work, we use $\alpha = 0.03$, which ensures that the turbulent heating term not excessively large, and results in the theoretical proton and electron temperatures being similar to the observed proton and electron temperatures. The second and third terms on the right-hand side (rhs) of Equation (12) are the turbulent shear source and the PUI source of turbulence. Similarly, the second term on the rhs of Equation (13) is the turbulent shear source. Zank et al. (2017) derived the turbulent shear source, which decreases as r^{-2} , and is different from that in Zank et al. (1996), Smith et al. (2006), and Breech et al. (2008), which decreases as r^{-1} , and is proportional to turbulence energy. The parameter ΔU is the difference between fast and slow solar wind speeds. Larrodera & Cid (2020) found that the fast and slow solar wind speeds are typically 500 ± 100 and 380 ± 40 km s⁻¹, respectively. We choose $\Delta U = 200 \text{ km s}^{-1}$, which is close to the value of Larrodera & Cid (2020). Furthermore, we assume ΔU to be a constant as we solve for a steady-state model. The parameter V_{A0} (= 45 km s⁻¹) is the Alfvén velocity at the reference point $r_0(=1 \text{ au})$. The parameters c^{\pm} and c_{E_D} are the parameterized strengths of the turbulent shear source, and f_D is the fraction of the PUI-driven turbulence source that drives turbulence in the outer heliosphere. It is assumed that the turbulent shear source supplies energy in equal amounts to the outward and inward Elsässer energies $(c^+ \sim c^-)$, and differently for the residual energy ($c^{\pm} \neq c_{E_n}$). Zank et al. (1996) estimated a crude value for the strength of the turbulent shear source to be \sim 13. Smith et al. (2006) used a reduced value of the strength of the turbulent shear source between 1 and 2. In this work, we use $c^{\pm} = 0.3$ and $c_{E_D} = 0.7$.

We also assume that the wave energy generated by PUIs is equal to the outward and inward Elsässer energy (Williams & Zank 1994). The PUI source of turbulence is not included in the transport equation of the residual energy because only Alfvénic fluctuations are assumed to be generated by PUIs (e.g., Adhikari et al. 2015). Isenberg et al. (2023) point out that

the energy released into fluctuations by the unstable scattering of PUIs is significantly lower than the standard bispherical prediction. The authors defined $f_D = (1 - Q_{\min})(U/V_A)$, where Q_{\min} is the minimum value of the normalized energy loss, and found that the f_D is reduced from the dispersive bispherical value of 0.642–0.06. We also use $f_D = 0.06$. The parameter $n_H^{\infty} = 0.127$ cm⁻³ is the interstellar H neutral density at the heliospheric termination shock (Swaczyna et al. 2020), $n_{\rm sw}^0 = 7$ cm⁻³ is the solar wind density at 1 au, $\tau_{\rm ion}^0 = 10^6$ s is the neutral ionization time at 1 au, and L = 5 au (Rucinski & Bzowski 1995) is the ionization cavity length scale. V_A' is the (azimuthal) Alfvén velocity. In the PUI source of turbulence term, U, V'_A , and the exponential function are radially dependent, which yields a PUI source of turbulence that is a function of distance. We couple the turbulence transport Equations (12)–(15) with a three fluid solar wind model.

4. Transport of Density Fluctuations

Equation (37) of Hunana & Zank (2010) describes the transport of density fluctuations ρ , and is given by

$$\frac{\partial \rho}{\partial t} + (\boldsymbol{U} + \boldsymbol{u}) \cdot \nabla \rho = -\rho \nabla \cdot \boldsymbol{u} - \chi \rho \nabla \cdot \boldsymbol{U}. \tag{16}$$

To derive the transport equation for the variance of the density fluctuations $\langle \rho^2 \rangle$, we multiply Equation (16) by ρ , use Equation (6), take an ensemble average, and assume isotropic turbulence. This yields the following equation:

$$\frac{\partial \langle \rho^2 \rangle}{\partial t} + \boldsymbol{U} \cdot \nabla \langle \rho^2 \rangle + 2 \langle \rho^2 \rangle \nabla \cdot \boldsymbol{U} = -\alpha_2 \frac{\langle u^2 \rangle^{1/2} \langle \rho^2 \rangle}{\lambda_u},$$
(17)

where α_2 is a von Kármán–Taylor constant. The parameters $\langle u^2 \rangle$ and λ_u are the fluctuating kinetic energy and the corresponding correlation length, and are given by Zank et al. (2012a) and Dosch et al. (2013)

$$\langle u^2 \rangle = \frac{\langle z^{+2} \rangle + \langle z^{-2} \rangle + 2E_D}{4} \quad \text{and}$$

$$\lambda_u = \frac{\langle z^{+2} \rangle \lambda^+ + \langle z^{-2} \rangle \lambda^- + E_D \lambda_D}{\langle z^{+2} \rangle + \langle z^{-2} \rangle + 2E_D}.$$
(18)

The 1D steady-state equation is given by

$$U\frac{d\langle \rho^2 \rangle}{dr} + 2\langle \rho^2 \rangle \frac{dU}{dr} + \frac{4U}{r} \langle \rho^2 \rangle$$

$$= -\alpha_2 \frac{\langle u^2 \rangle^{1/2} \langle \rho^2 \rangle}{\lambda_u}$$

$$+ \eta_1 \langle \rho^2 \rangle_0 \frac{r_0^2 |\Delta U|}{r^3} + \eta_2 \langle \rho^2 \rangle_0 \frac{U}{V_A} \frac{n_H}{\tau_{\text{ion}}^0 n_{\text{sw}}^0} \exp\left(\frac{-L}{r}\right). \tag{19}$$

Equation (19) includes a turbulent shear source (the second term on the rhs) and a PUI source of turbulence (the third term on the rhs) (see also, Zank et al. 2012b, 2017). The parameters η_1 and η_2 determine the strength of the turbulent shear source and the PUI source of turbulence. Zank et al. (2017) suggested the values for $\eta_1 = 10^{-3} - 10^{-2}$ and $\eta_2 = 10^{-4} - 10^{-3}$. However, we use $\eta_1 = 1.8 \times 10^{-4}$ and $\eta_2 = 1.5 \times 10^{-10}$. Zank et al. (2017) had introduced η_2 as a possible source of density

turbulence associated with PUI driving of Alfvén waves. Although Alfvén waves, being incompressible, do not generate compressible fluctuations, Zank et al. (2017) pointed out that there might be a pseudosound contribution to the density fluctuations, i.e., the Alfvén waves might excite low-frequency sound waves (Zank & Matthaeus 1992b), but this was only speculation added for completeness. The small value of η_2 indicates that the pseudosound correction to the density fluctuations is too small to be important. $\langle \rho^2 \rangle_0$ is the variance of the density fluctuations at 1 au. Notice that the first term on the rhs of Equation (19) is a nonlinear term, which couples the transport equations of the density variance with the turbulence transport equations.

5. Three Fluid Solar Wind Model

We extend the solar wind model developed by Zank et al. (2018b) to include electrons as a separate fluid. The 1D steady-state solar wind proton (ρ_s) continuity equation and the PUI (proton, ρ_p) continuity equation can be written as

$$\frac{1}{r^2}\frac{d}{dr}(r^2\rho_s U) = -\nu_c^s \rho_s; \tag{20}$$

$$\frac{1}{r^2} \frac{d}{dr} (r^2 \rho_p U) = \nu_c^s \rho_s + S_p^{\text{ph}} = \nu_c^s \rho_s + \nu_{p0} m_p N \left(\frac{r_0}{r}\right)^2, \quad (21)$$

respectively, where the rhs term in Equation (20) and the first term on the rhs of Equation (21) denote the charge exchange between the solar wind protons and the interstellar hydrogen neutrals. Here the charge exchange term acts as a sink for the solar wind proton continuity equation, and acts as a source for the PUI continuity equation (see Zank 1999 for further details). The second term on the rhs of Equation (21) denotes the photoionization of the interstellar neutrals $(S_p^{\rm ph})$. The ionization rate is given by $\nu_{p0} = 1.5 \times 10^{-7} \ {\rm s}^{-1}$ (Axford 1972), m_p is the proton mass, and N,

$$N(r) = n_{\rm H}^{\infty} \exp\left(\frac{-L}{r}\right) \tag{22}$$

is the radially varying neutral H number density (Vasyliunas & Siscoe 1976). The charge-exchange rate ν_c^s between solar wind protons and interstellar H neutrals is (Holzer 1972)

$$\nu_c^s \equiv \nu_{c0} N \left[\frac{128k_B}{9\pi m_p} (T_s + T_{\rm H}) + (U - U_{\rm H})^2 \right]^{1/2}, \qquad (23)$$

where $\nu_{c0} = 2 \times 10^{-15}$ cm² is the charge-exchange cross section, k_B is Boltzmann's constant, T_s is the solar wind proton temperature, $T_{\rm H} = 6500$ K is the neutral H temperature, and $U_{\rm H} = 20$ km s⁻¹ is the drift speed.

The 1D steady-state momentum equation can be written as

$$\rho_{s}U\frac{dU}{dr} + \frac{dP_{s}}{dr} + \frac{dP_{e}}{dr} + \frac{dP_{p}}{dr} + \frac{B}{\mu_{0}}\frac{dB}{dr}
= S_{p}^{ph}(U_{H} - U) + (\nu_{c}^{s}\rho_{s} + \nu_{c}^{p}\rho_{p})(U_{H} - U),$$
(24)

where P_s , P_e , and P_p denote the solar wind proton pressure, the solar wind electron pressure, and the PUI pressure,

respectively. B is the azimuthal magnetic field, and is given by

$$\frac{1}{r}\frac{d}{dr}(rUB) = 0; \ \frac{B(r)}{B_0} = \frac{r_0}{r} \left(\frac{U}{U_0}\right)^{-1},\tag{25}$$

where B_0 is the magnetic field and U_0 is the solar wind speed at a reference point r_0 . Equation (25) is derived from Maxwell's equation by taking the azimuthal component. The charge-exchange rate ν_c^p between PUIs and interstellar H neutrals is (Holzer 1972)

$$\nu_c^p = \nu_{c0} N \left[\frac{128k_B}{9\pi m_p} (T_p + T_{\rm H}) + (U - U_{\rm H})^2 \right]^{1/2}.$$
 (26)

The 1D steady-state transport equation for the P_s , P_e , and P_p can be expressed as

$$U\frac{dP_s}{dr} + \gamma_s P_S \frac{dU}{dr} + 2\gamma_s \frac{U}{r} P_s$$

$$= (\gamma_s - 1) [\nu_{se}(P_e - P_s) + f_p S_t] - \nu_c^s \rho_s \frac{k_B T_s}{m_e}; \qquad (27)$$

$$U\frac{dP_e}{dr} + \gamma_e P_e \frac{dU}{dr} + 2\gamma_e \frac{U}{r} P_e$$

=(\gamma_e - 1)[\nu_{es}(P_s - P_e) - \nabla \cdot \mathbf{q}_e + (1 - f_p)S_t]; (28)

$$\begin{split} &U\frac{dP_{p}}{dr} + \gamma P_{p}\frac{dU}{dr} + 2\gamma \frac{U}{r}P_{p} \\ &= &(\gamma_{p} - 1)(S_{p}^{\text{ph}} + \nu_{c}^{s}\rho_{s} + \nu_{c}^{p}\rho_{p}) \left(\frac{1}{2}(U_{\text{H}} - U)^{2} + \frac{3}{2}\frac{k_{B}T_{\text{H}}}{m_{p}}\right) \\ &- \nu_{c}^{p}\rho_{p}\frac{k_{B}T_{p}}{m_{p}}, \end{split} \tag{29}$$

where $\gamma_s (\equiv \gamma_e = \gamma_p) = 5/3$ is the adiabatic index, $f_p (\equiv 0.6)$ is the fraction of the dissipated turbulence energy that is used to heat the solar wind protons, and $(1 - f_p)$ is the fraction of the dissipated turbulence energy that is used to heat the solar wind electrons (Breech et al. 2009). The viscous and heat flux terms, at least in the context of the thermal solar wind ions, are expressed in terms of the Navier-Stokes equations. These are derived under the assumption of strong collisionality, which is not reasonable in the supersonic solar wind. The precise mechanism by which the energy in fluctuations is converted to heat the solar wind is an active area of research, but the approach implicit in the turbulence transport formulation (here and in all prior models) is that the large-scale rate of energy transfer that is described by the turbulence transport formalism is equal to the dissipation rate (i.e., assuming fully developed turbulence or Kolmogorov turbulence). This allows us to sidestep the physics of the dissipation itself since the rate of dissipation is computed. This therefore allows us to neglect specific (unknown) dissipation terms in the solar wind equations describing the ions. Zank et al. (2014) derived the wave-particle interaction heat conduction and viscosity terms for the PUIs. However, for the reasons outlined in Zank et al. (2018b) (considering larger scales than the viscous and heat conduction PUI length/timescales), we neglect the dissipative heating effects.

By contrast, the electron heat flux cannot easily be neglected because the electron strahl is extremely extended in spatial extent. Accordingly, we retain the heat flux term for electrons, albeit very simplified. The heating term S_t can be written as (Verdini et al. 2010; Adhikari et al. 2022c)

$$S_t = \alpha m_p n_s \left[\frac{\langle z^{+2} \rangle \langle z^{-2} \rangle^{1/2}}{\lambda^+} + \frac{\langle z^{-2} \rangle \langle z^{+2} \rangle^{1/2}}{\lambda^-} \right]. \tag{30}$$

The collisional frequency v_{se} between solar wind protons and solar wind electrons is given by Zank (2014)

$$\nu_{se} = \frac{2n_e q_p^2 q_e^2 \log \Lambda}{4\pi \epsilon_0^2 m_p^2 \nu_{T_p}^2} \frac{T_p}{T_e} \frac{G(x_e)}{x_p},$$
(31)

where n_e is the electron density, q_p is the proton charge (e), q_e is the electron charge (-e), ϵ_0 is the permittivity of free space, ν_{Tp} is the thermal proton speed, T_p is the proton temperature, T_e is the electron temperature, $x_e = \nu/\nu_{Te}$, and $x_p = \nu/\nu_{Tp}$. $G(x_e)$,

$$G(x_e) \sim \begin{cases} \frac{2x_e}{3\sqrt{\pi}}, & \text{for } x_e \ll 1\\ \frac{1}{2x_e^2}, & \text{for } x_e \gg 1, \end{cases}$$
(32)

is the Chandrasekhar function. For $x_e \ll 1$ (Zank et al. 2014), Equation (31) simplifies to

$$\nu_{se} = \frac{n_e}{T_c^{3/2}} \log \Lambda \times 1.97 \times 10^{-3} \,\mathrm{s}^{-1},\tag{33}$$

which is similar to Equation (13) of Cranmer et al. (2009). We use $\log \Lambda = 2$. According to Cranmer et al. (2009), we assume that $\nu_{se} \sim \nu_{es}$, and $n_e \sim n_s + n_p$ (to ensure charge neutrality). The electron heat flux is given by the empirical formula (Cranmer et al. 2009)

$$\ln\left(\frac{q_{\parallel,e}}{q_0}\right) = -0.7037 - 2.115x - 0.2545x^2,\tag{34}$$

where $x \equiv \ln(r/1\text{au})$ and $q_0 = 0.01$ erg cm⁻²s⁻¹.

6. Evolution of Turbulence from 1-75 au

The 1D steady-state Equations (12)–(15) describe the radial evolution of turbulence. Similarly, the 1D steady-state Equations (20), (21), (24), (27)–(29) describe the radial evolution of the solar wind and PUI density, solar wind speed, proton and electron pressures, and PUI pressure. Using the boundary conditions shown in Table 1, and the parameter values shown in Table 2, we solve the coupled 1D steady-state NI MHD turbulence equations and the solar wind (protons and electrons) + PUI equations from 1–75 au. The boundary conditions are chosen within the error bar of the observed values, where the error bar represents the standard deviation. The parameter values used in the model yield unique solutions, and are similar to the observed values. In Figures 1 and 2, the theoretical turbulence energies (solid curve), and the corresponding theoretical correlation lengths (solid curve) are compared with the Voyager 2 (V2) measurements (blue circle). Using V2 magnetic field and plasma data from the years 1977-2004, we calculate the observed transverse turbulence energy and the observed transverse correlation length. To calculate the observed turbulence energy, we consider 10 hr long data sets (e.g., Zank et al. 1996). If there are at least five good data points, we calculate the fluctuating radial, tangential,

Table 1Boundary Values of the SW + PUI Parameters and the Turbulence Quantities at 1 au

Turbulence	Boundary Values	Observed Values $\pm \sigma$	SW+PUI	Boundary Values	Observed Values $\pm \sigma$
$\langle z^{+2} \rangle \text{ (km}^2 \text{ s}^{-2})$	740	372.45 ± 373.68	$U (\mathrm{km \ s^{-1}})$	410	371.38 ± 43.77
$\langle z^{-2} \rangle \text{ (km}^2 \text{ s}^{-2})$	1650	940.98 ± 754.77	$n_s (\mathrm{cm}^{-3})$	7	10.45 ± 7.03
$E_D (\mathrm{km^2 s^{-2}})$	-200	-195.28 ± 274.68	$n_p ({\rm cm}^{-3})$	5.13×10^{-7}	
λ^+ (km)	1.4×10^{6}	$(1.55 \pm 1.33) \times 10^6$	P_s (Pa)	5.79×10^{-12}	$(9.66 \pm 9.18) \times 10^{-12}$
λ^{-} (km)	1.6×10^{6}	$(1.32 \pm 0.67) \times 10^6$	P_e (Pa)	2.89×10^{-12}	•••
λ_D (km)	10×10^{6}	$(11.48 \pm 7.76) \times 10^6$	P_p (Pa)	4.62×10^{-23}	•••
$\langle \rho^2 \rangle \text{ (cm}^{-6})$	10	8.32 ± 20.95			•••

Note. The third column denotes the mean and standard deviation σ of the observed value.

 Table 2

 Values of the Parameters Used for the Turbulence Model

Parameters	Values	Parameters	Values
a	1/2	c^+	0.3
b	1/2	c^{-}	0.3
α	0.03	c_{ED}	0.7
β	0.015	α_2	0.05
V_{A0}	$45 \text{ (km s}^{-1}\text{)}$	η_1	1.8×10^{-5}
ΔU	$200 \text{ (km s}^{-1}\text{)}$	η_2	1.5×10^{-10}
f_D	0.06	•••	

and normal (R, T, N) components of the magnetic field and the solar wind speed in the direction perpendicular to the mean magnetic field (Adhikari et al. 2022c). Then, we calculate the variance of the perpendicular fluctuating components to obtain the transverse turbulence energy. Also, we calculate the mean value of the solar wind parameters corresponding to this interval. After this, we use 65 sequential data points from 1977–2004 to calculate the mean and standard deviation of the relevant quantities. For the transverse correlation length, we consider a longer 20 hr interval consisting of 20 good points to generate a reasonable auto-correlation function with time lag τ . We convert the time lag τ into the spatial lag distance by Taylor's hypothesis. We then use a cubic spline data interpolation to fit the auto-correlation function, from which the correlation length is determined. The correlation length is obtained by finding the lag distance at which the autocorrelation function becomes 1/e of the maximum autocorrelation function corresponding to a zero lag. Finally, we smooth the observed correlation length by calculating the mean and standard deviation over the distance dr = 0.5 au. In Table 1, the mean and standard deviation corresponding to the observed turbulence energy and solar wind parameters correspond to a distance of 1.01 au. Similarly, the mean and standard deviation corresponding to the observed correlation length corresponds to a distance of 1.18 au.

The top left panel of Figure 1 compares the theoretical and observed outward Elsässer energy $\langle z^{+2} \rangle$ as a function of distance from 1–75 au. The theoretical and observed $\langle z^{+2} \rangle$ decreases with increasing distance until ~25 au, and then flattens with distance. In the top right panel of Figure 1, we plot the theoretical inward Elsässer energy $\langle z^{-2} \rangle$ and the observed $\langle z^{-2} \rangle$ as a function of distance. Both the theoretical and observed $\langle z^{-2} \rangle$ show similar radial profiles with increasing distance. The flattening of the $\langle z^{+2} \rangle$ and $\langle z^{-2} \rangle$ in the outer heliosphere is due to the PUI-driven turbulence in the outer heliosphere (the third term on the rhs of Equation (12)).

The cross-helicity measures the difference between the outward and inward Elsässer energies. The observed normalized cross-helicity σ_c is about -0.38 at 1 au, and increases slowly with distance (the middle left panel of Figure 1). The theoretical σ_c is consistent with that observed from 1–75 au.

The residual energy is defined as the difference between the fluctuating kinetic energy and the fluctuating magnetic energy. The middle right panel of Figure 1 shows that the observed σ_D is about -0.28 at 1 au, and decreases slowly until $\sim\!20$ au, and then increases as a function of distance. Similarly, the theoretical σ_D decreases gradually until $\sim\!15$ au, and then increases with distance. The theoretical σ_D is negative from 1–75 au, indicating the dominating fluctuating magnetic energy compared to the fluctuating kinetic energy. The observed σ_D is clearly negative until $\sim\!40$ –50 au, and then the observed σ_D can also become positive.

The bottom left panel of Figure 1 shows that the theoretical $\langle B^2 \rangle$ is in good agreement with the observed $\langle B^2 \rangle$ from 1–75 au. Similarly, in the bottom right panel, the theoretical $\langle u^2 \rangle$ decreases from 1 to 20 au, and then increases slightly as distance increases. This may be due to the turbulence driven by PUIs in the outer heliosphere, which leads the fluctuations to be in the equipartitioned state between the fluctuating kinetic and magnetic energy. The theoretical $\langle u^2 \rangle$ shows good agreement with the observed $\langle u^2 \rangle$.

The left panel of Figure 2 shows the ratio between the square root of the fluctuating magnetic energy and the background magnetic field $\langle B^2 \rangle^{1/2}/B$ as a function of heliocentric distance. The solid curve denotes the theoretical result and the open circles the observed values. The theoretical $\langle B^2 \rangle$ is calculated from $\langle B^2/\mu_0\rho\rangle = (\langle z^{+2}\rangle + \langle z^{-2}\rangle - 2E_D)/4$. The theoretical large-scale magnetic field is calculated from $B = B_a (r_a/r)^2 [1 + (\Omega r/U)^2 (1 - (r_a/r)^2)^2 \sin^2 \theta]^{1/2}$ (Weber & Davis 1967), where $\Omega = 2.9 \times 10^{-6} \text{ rad s}^{-1}$, and $\theta = 90^{\circ}$. We use $B_a = 1.6 \times 10^3$ nT at $r_a = 10$ R_{\odot} , so the theoretical magnetic field is similar to that of V2 (not shown in this manuscript). Both the theoretical and observed result show that $\langle B^2 \rangle^{1/2}/B$ approximately constant between 1 and 2 au, and then decreases with increasing distance. However, Chhiber (2022) found that $\langle B^2 \rangle^{1/2}/B$ increases radially in the inner heliosphere using PSP data sets. The difference between within and outside of 1 au is because the magnetic field is mainly dominated by the radial component $(\sim r^{-2})$ in the inner heliosphere, and the azimuthal component $(\sim r^{-1})$ in the outer heliosphere.

In the right panel of Figure 2, we plot the theoretical and observed ratio between the square root of the fluctuating kinetic energy and the background solar wind speed $\langle u^2 \rangle^{1/2}/U$ between 1 and 75 au, which decreases from 1 to \sim 20 au, and then increases with distance.

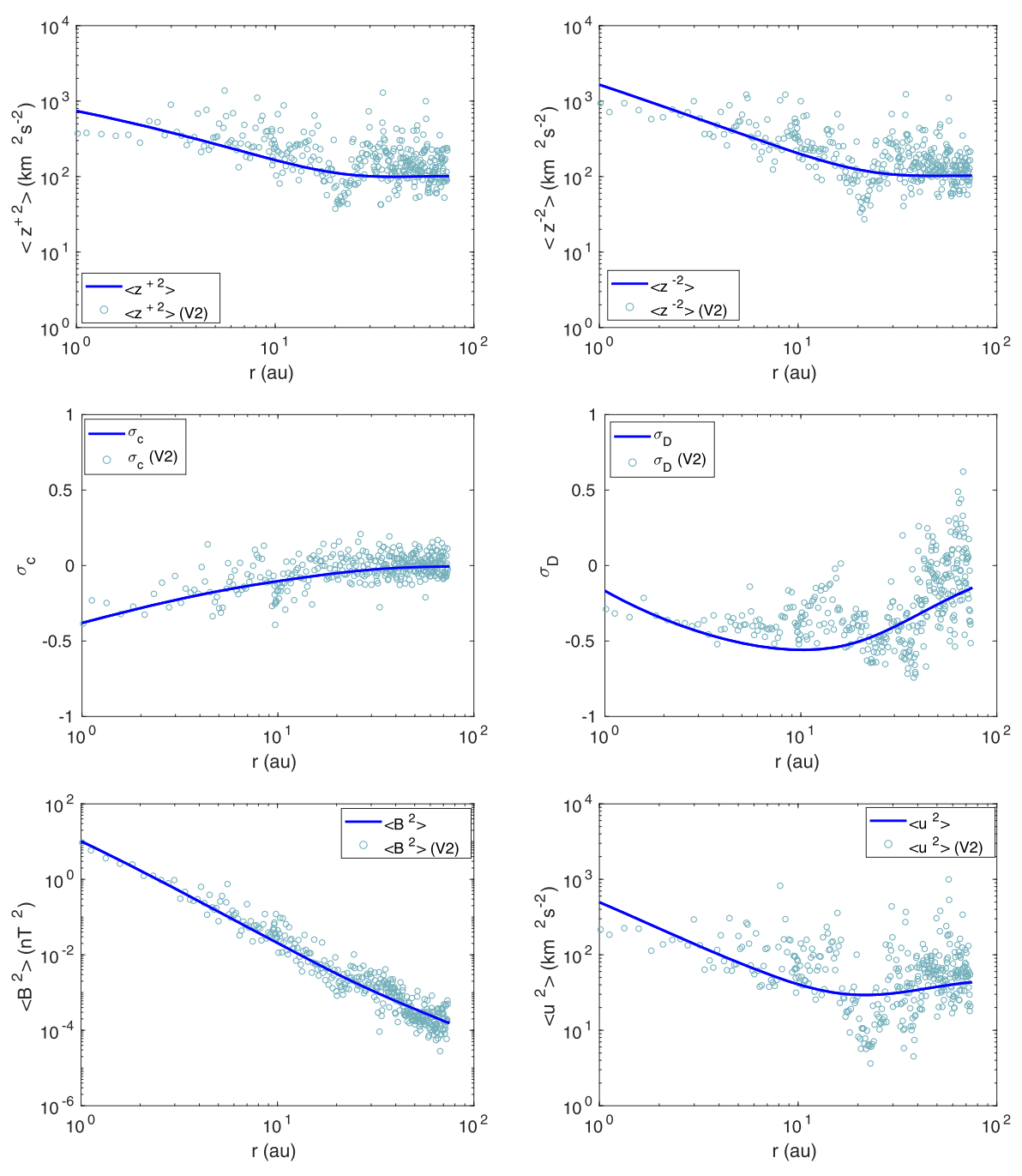


Figure 1. Comparison between the theoretical and observed turbulence energies as a function of heliocentric distance. Top left and right panels illustrate the outward and inward Elsässer energies. Middle left and right panels show the normalized cross-helicity and the normalized residual energy. Bottom left and right panels show the fluctuating magnetic energy and the fluctuating kinetic energy. The solid curve denotes the theoretical result. The open circles denote observed values by V2.

The left panel of Figure 3 illustrates the variance of the density fluctuations with distance. The theoretical and observed results decrease as $r^{-4.48}$ and $r^{-4.71}$, respectively. Here, the variance of the density fluctuations decreases more rapidly than r^{-4} , which is the approximate square of the radial dependence of the proton density. This is because the density fluctuations driven by the passive scalar velocity fluctuations lead to the reduction of the density fluctuations (see also Zank et al. 2017). Therefore, the ratio between the square root of the variance of the density fluctuations and the mean proton density decreases with increasing distance, as shown in the right panel of Figure 3. In the figure, the observed ratios (open blue circles) are widely dispersed, which may be related to the presence of a

periodic density structure (Di Matteo et al. 2019; Kepko et al. 2020). The theoretical ratio increases slightly beyond $\sim\!60\,\mathrm{au}$.

The top left panel of Figure 4 shows the radial evolution of the correlation length of the outward Elsässer energy λ^+ . The observed λ^+ increases gradually until $\sim\!20\,\mathrm{au}$, and then decreases. The theoretical λ^+ also increases monotonically until $\sim\!20\,\mathrm{au}$, and then decreases slightly. Similarly, the top right panel of Figure 4 shows that the theoretical and observed correlation length of the inward Elsässer energy λ^- increases gradually until $\sim\!20\,\mathrm{au}$, and then decreases with increasing distance.

The middle left panel of Figure 4 compares the theoretical and observed correlation length of the residual energy. The

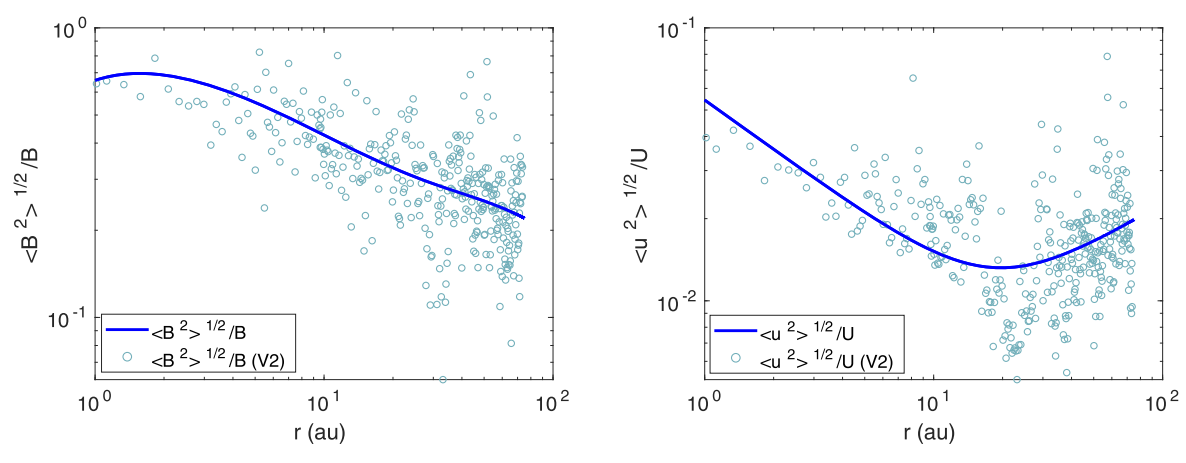


Figure 2. Comparison between the theoretical and observed ratio between the square root of the fluctuating magnetic energy and magnetic field (left), and between the square root of the fluctuating kinetic energy and solar wind speed (right) as a function of heliocentric distance. The format of the figure is similar to Figure 1.

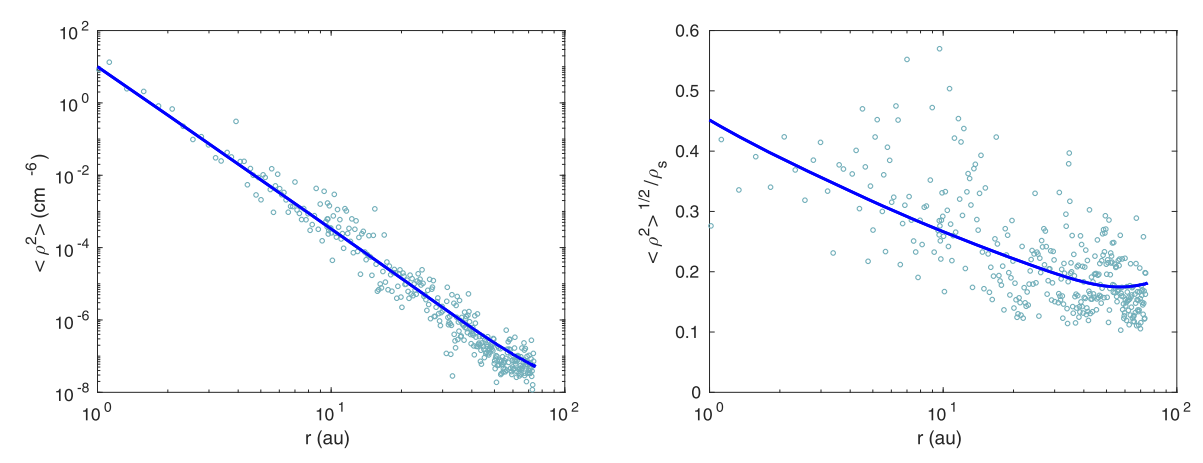


Figure 3. Left: comparison between the theoretical and observed variance of density fluctuations as a function of distance. Right: comparison between the theoretical and observed ratio between the square root of the variance of density fluctuations and the background density as a function of distance. The format of the figure is similar to that of Figure 1.

theoretical λ_D decreases initially, which may be due to the turbulence shear source. As the strength of the turbulent shear source term decreases with distance, the theoretical λ_D increases gradually. The difference between the observed and theoretical values may suggest that the turbulent shear source term should be smaller than it is currently in the residual energy equation and the correlation length of the residual energy. For example, it is possible that the Kelvin-Helmholtz instability may drive more Alfvénic fluctuations than 2D structures in a high beta plasma and thus a different parameterization of the shear driving source term than used in Adhikari et al. (2017a) and Zank et al. (2017) may be necessary. The observed λ_D is approximately constant as a function of distance. The middle right panel of Figure 4 shows that the theoretical and observed λ_b increases monotonically with distance until ~ 20 au, and then decreases slightly. The bottom panel compares the theoretical and observed correlation length of the velocity fluctuations λ_u . The theoretical $\lambda_u = (\langle z^{+2} \rangle \lambda^+ + \langle z^{-2} \rangle \lambda^- + E_D \lambda_D)/(\langle z^{+2} \rangle + \langle z^{-2} \rangle + 2E_D))$, which depends on the turbulence energies and the correlation lengths, increases with increasing distance, while the observed λ_u is approximately constant as a function of distance. The differences between the theoretical and observed λ_D and λ_u may be due to the turbulent shear source that was derived in the context of the low plasma beta models (Zank et al. 2017). The turbulent shear source

parameters may need to be changed for a high plasma beta model by generating similar amounts of 2D and Alfvénic fluctuations.

7. Radial Evolution of Solar Wind Background Profile

The left panel of Figure 5 compares the theoretical and observed solar wind proton density (blue curve, and blue and yellow circles, respectively), and the theoretical and observed PUI density (red curve and open red triangles, respectively) as a function of distance.

The theoretical proton density shows good agreement with the observed proton density measured by V2 (blue circles) and NH SWAP (yellow circles). In the model, PUIs are produced by charge exchange between solar wind protons and interstellar H neutrals, and photoionization of the interstellar H neutrals (see Zank 1999). The theoretical result shows that at 1 au, the PUI density is about 5×10^{-7} cm⁻³, which increases to a peak value of $\sim 10^{-3}$ cm⁻³ at ~ 8 au, and then decreases slowly with distance (see also, Zhao et al. 2019). The theoretical PUI density is consistent with the observed PUI density measured by NH SWAP.

In the PUI pressure equation, the PUI viscosity and the PUI heat conduction are neglected. We also do not include any heating term in the PUI pressure equation. The right panel of

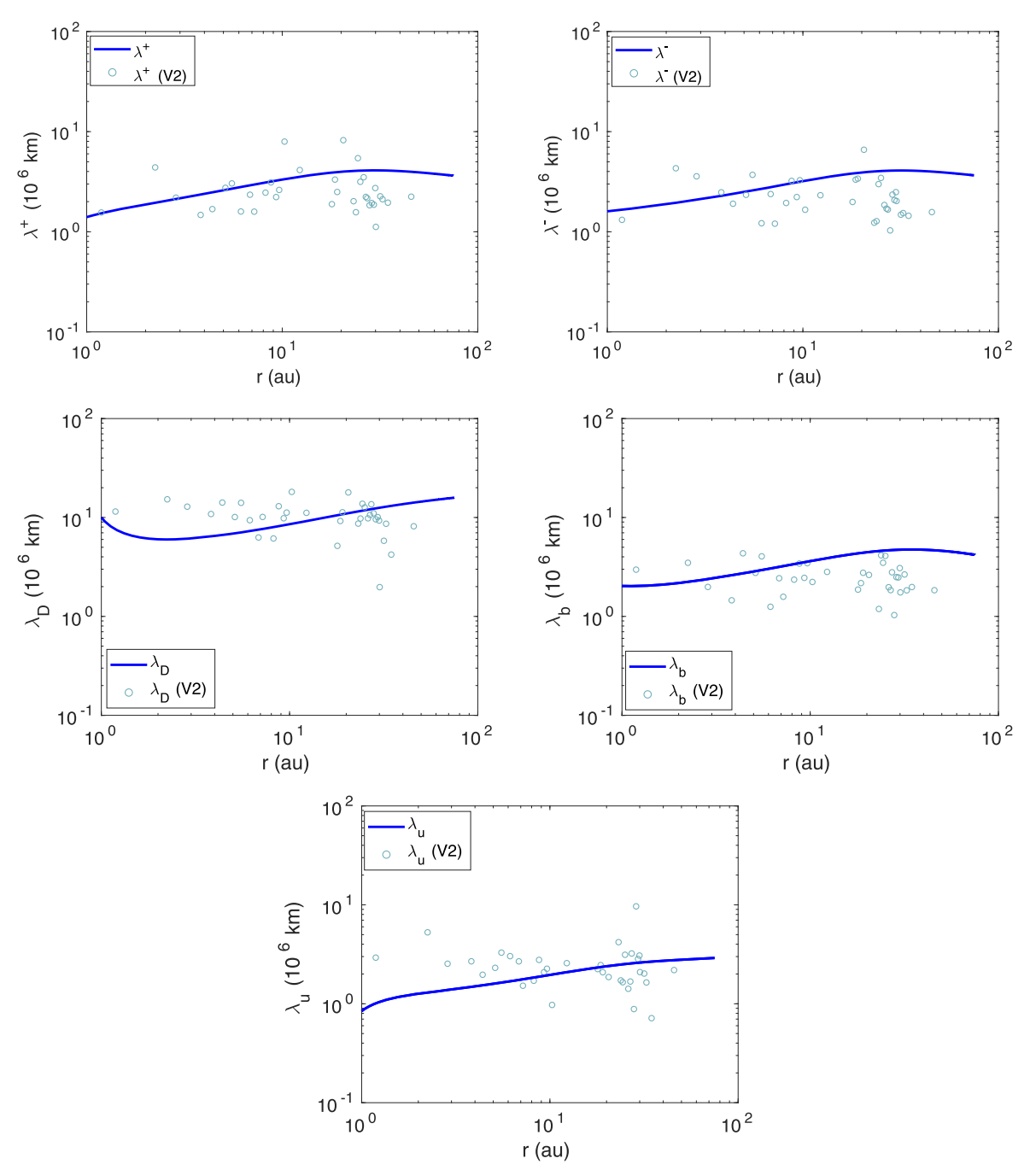
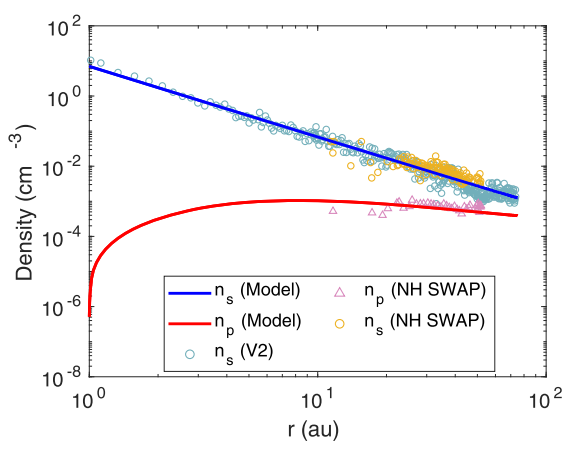


Figure 4. Comparison between the theoretical and observed correlation lengths as a function of distance. Top left and right panels show the correlation length corresponding to the outward and inward Elsässer energies. Middle left and right panels show the correlation length corresponding to the residual energy and fluctuating magnetic energy. Bottom panel illustrates the correlation length of velocity fluctuations. The format of the figure is similar to Figure 1.

Figure 5 shows that the theoretical PUI temperature (red curve) decreases gradually as $r^{-0.18}$. The observed PUI temperature (open red triangles) decreases gradually from $\sim \! 10$ to 30 au, then increases to a peak value of 5.1×10^6 K, and then decreases again with distance. The theoretical PUI temperature is in reasonable agreement with the observed PUI temperature between $\sim \! 11$ and 52 au. For the solar wind proton and electron pressure equations, we distribute turbulence energy in the ratio of 60:40. In the outer heliosphere, PUIs are one of the main components of the solar wind plasma and generate turbulence. As a result, the solar wind proton and electron temperatures increase in the outer heliosphere, which is also confirmed by the theoretical and observed results in the right panel of

Figure 5. The theoretical solar wind proton temperature (blue curve) is in reasonable agreement with the observed proton temperature (open blue circles). The theoretical solar wind electron temperature increases initially due to the electron heat flux (see Breech et al. 2009; Adhikari et al. 2021a), and decreases until \sim 20 au, and then increases as a result of the dissipation of PUI-driven turbulence in the outer heliosphere. The theoretical electron temperature (green curve) is consistent with the observed electron temperature (filled blue circle) measured by Ulysses near the ecliptic plane between 4 and 6 au.

Figure 6 shows the plasma beta as a function of heliocentric distance. The theoretical proton plasma beta (blue curve)



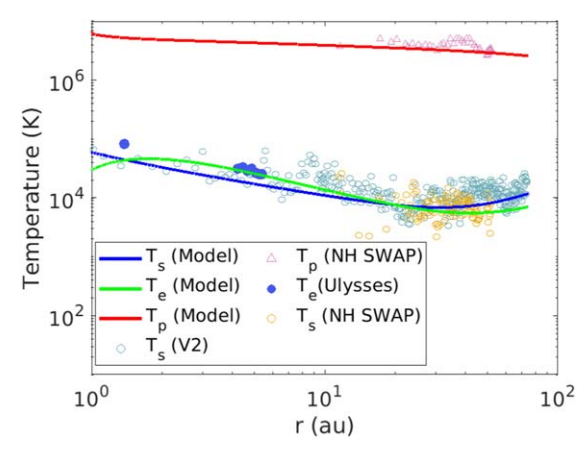


Figure 5. Left: comparison between the theoretical and observed solar wind density, and the theoretical and observed PUI density as a function of distance. Right: comparison between the theoretical and observed solar wind proton temperature, the theoretical and observed electron temperature, and the theoretical and observed PUI temperature with increasing distance. Red and blue curves denote the theoretical results. Open red triangles, open blue circles, open yellow circles, and filled blue circles denote the observed results.

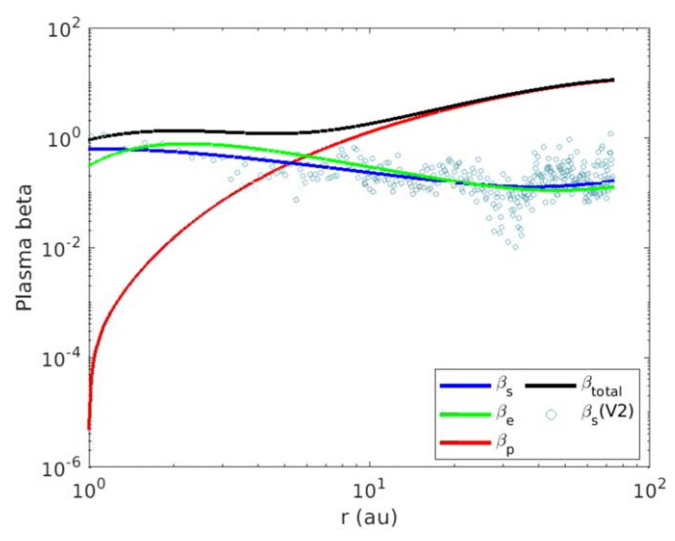


Figure 6. Plasma beta as a function of heliocentric distance. Blue and green curves denote the theoretical proton and electron plasma beta. Red curve denotes the theoretical PUI plasma beta. The black curve denotes the theoretical total plasma beta. Blue circles denote V2 measured proton plasma beta.

decreases with distance until $\sim 30\,\mathrm{au}$, and then increases, similar to that measured by V2 (blue circles). The theoretical electron plasma beta (green curve) is approximately similar to the theoretical proton plasma beta. The theoretical PUI plasma beta (red curve) is about 5×10^{-6} at 1 au and increases to 11.4 at 75 au. The total plasma beta (black curve) is about 1 between 1 and 10 au, and about 11.4 at 75 au.

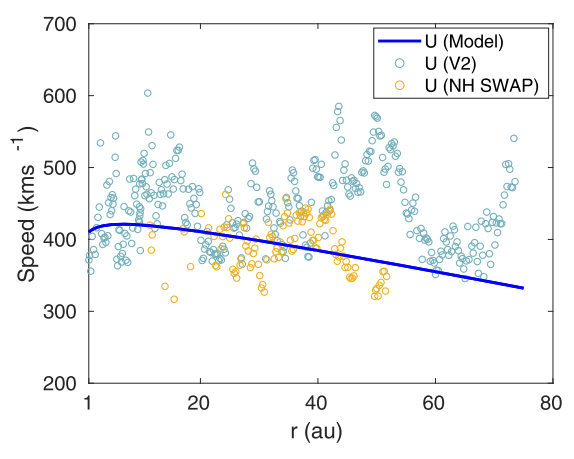
The pickup process takes energy and momentum from the solar wind (Zank 1999), which results in its speed decreasing gradually in the outer heliosphere (blue curve in the left panel of Figure 7, see also Lee 1995; Richardson et al. 1995; Richardson & Wang 2003; Zank et al. 2018b; Elliott et al. 2019). The theoretical solar wind speed between ~42 and 58 au tracks the NH SWAP measured speed (open yellow circles) more closely than the V2 measured speed (open blue circles). The (time-dependent) simulation result of solar wind speed obtained by Korolkov & Izmodenov (2022) also deviates from the V2 measured speed in this region. The solar wind speed measured by NH SWAP and V2

in the years 2018–2021 and 1995–1999, respectively, occurs in the solar minimum of solar cycles 23 and 25. However, V2 was located outside the sector zone in the high-speed streams of the solar wind (Burlaga et al. 2003). Between 25 and 40 au, Richardson et al. (1995) found a 6% decrease in the solar wind speed, consistent with the 5%–7% reported by Elliott et al. (2019) at distances from 30–43 au. Wang et al. (2000) reported that the speed decreases by about 10% at 60 au. In the right panel of Figure 7, we plot the percentage decrease in solar wind speed as a function of distance. Initially, the percentage speed change is positive because the flow is driven by the gradient in the solar wind proton pressure, the solar wind electron pressure, and the PUI pressure, and then decreases after the PUIs influence the solar wind plasma. The solar wind speed decreases by about 19% at 75 au.

8. Discussion and Conclusions

Using NI MHD phenomenology (Zank et al. 1990; Zank & Matthaeus 1993; Hunana & Zank 2010), we developed a new turbulence transport model for the high plasma beta $(\beta \gg 1)$ regime. The leading-order turbulence transport equations in the high plasma beta regime include the Alfvén velocity and are fully 3D (Zank & Matthaeus 1993) unlike the NI MHD in the $\beta \sim 1$ and ≪1 regimes (see Zank et al. 2017; Wang et al. 2022). Equation (7) is the transport equation for the Elsässer variables, which is derived only from the leading-order (incompressible) description, takes into account the inhomogeneity, and completely eliminates compressibility. In the incompressible MHD description, the transport equation for the Elsässer variables is derived from the fluctuating components without separating the leading order and higher order. We remind readers that in the NI MHD description, the fluctuating solar wind speed is not solenoidal unlike in the incompressible MHD description. This leads to Equation (7) being different from that of Zhou & Matthaeus (1990a, 1990b), and Marsch & Tu (1989). Similarly, the six coupled turbulence transport Equations (8)-(11) or (12)-(15) are different from those of Zank et al. (2012a), who used an incompressible MHD phenomenology (Marsch & Tu 1989; Zhou & Matthaeus 1990a, 1990b).

We incorporated the newly developed turbulence transport model equations with a three fluid (proton, electron, and PUI) solar wind model. We compared the theoretical results with the



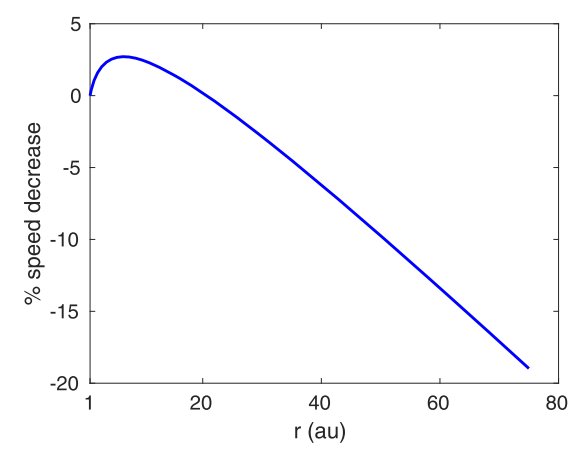


Figure 7. Left: comparison between the theoretical and observed solar wind speed as a function of distance. The blue curve denotes the theoretical result, and the open blue and yellow circles the observed speed. Right: the percentage decrease in solar wind speed as a function of distance.

observed results measured by V2, Ulysses, and NH SWAP. Note that the observed turbulence energy and the observed correlation length correspond to the transverse components (Adhikari et al. 2022c), and were calculated from V2 measurements. We summarize our findings as follows.

- 1. The theoretical fluctuating magnetic energy, fluctuating kinetic energy, and outward/inward Elsässer energy are similar to the corresponding observed turbulence energy. The theoretical results use fixed boundary conditions, and are therefore independent of solar cycle. However, the observed turbulence energy measured by V2 may reflect the influence of solar cycle (e.g., Zhao et al. 2018). Adhikari et al. (2014) used the time-dependent boundary conditions and turbulence sources in a 1D time-dependent solar wind and coupled to the magnetic turbulence model of Zank et al. (1996) to show that the fluctuating magnetic energy density varies periodically in the outer heliosphere.
- 2. The theoretical normalized residual energy decreases until ~ 20 au, and then increases due to the PUI-driven turbulence. The radial profile of the theoretical σ_D is similar to the radial profile of the observed σ_D . At 1 au, Zhao et al. (2018) found that the observed normalized residual energy was more negative, i.e., dominated by fluctuating magnetic energy, during solar maximum than during solar minimum. The observed σ_D measured by V2 may reflect this feature in the outer heliosphere.
- 3. The ratio between the square root of the fluctuating magnetic energy and the background magnetic field is approximately constant between 1 and 2 au, and then decreases with distance, which is different from that in the inner heliosphere, where the ratio increases (Chhiber 2022).
- 4. The ratio between the square root of the fluctuating kinetic energy and the solar wind speed decreases until $\sim\!20\,\mathrm{au}$, and then increases, which may be related to the deceleration of the solar wind speed in the outer heliosphere.
- 5. The variance of the density fluctuations decreases more rapidly than r^{-4} . The ratio between the square root of the variance of density fluctuations and the background density decreases with increasing distance until 50 au, and then increases slightly. The observed result shows a large variation, which may be due to the presence of a

- periodic density structure (Di Matteo et al. 2019; Kepko et al. 2020).
- 6. The theoretical and observed correlation length of the fluctuating magnetic energy, and the outward and inward Elsässer energy increases gradually with distance until \sim 20 au, and then decreases slightly with distance.
- 7. The inclusion of PUIs results in the solar wind speed decelerating in the outer heliosphere. The speed decreases by about 19% at 75 au (see also Richardson et al. 1995; Wang et al. 2000; Elliott et al. 2019).
- 8. The solar wind protons and electrons were heated by the dissipation of turbulence energy at the ratio of 60:40 (Breech et al. 2009), yielding theoretical proton and electron temperatures similar to those observed. In the PUI pressure equation, the PUI viscosity and the PUI heat conduction were neglected, and dissipation of turbulence was not included. The theoretical PUI temperature is in reasonable agreement with the observed PUI temperature between \sim 10–52 au and it is unclear that heating of PUIs occurs through the dissipation of turbulence. Recently, McComas et al. (2022) reported observations of several PUI-mediated shocks with compression ratios between 1.2 and 1.8 in the outer heliosphere. They found that PUIs are preferentially compressed and heated across the shock. However, since the shocks are weak, the downstream PUI temperature is not greatly enhanced compared to the upstream PUI temperature (McComas et al. 2022). This does not affect the results presented in the manuscript as we studied the evolution of large-scale turbulence and the background solar wind and PUI profiles.
- 9. The proton and electron plasma beta are less than 1 between 1 and 75 au. The PUI plasma beta is less than 1 within 10 au, and larger than 1 after 10 au. The total plasma beta is about 1 between 1 and 10 au, and increases to \sim 11.4 at 75 au.

We tested the new NI MHD turbulence transport model equations in the high plasma beta regime against V2 measurements. The comparison between the theoretical and observed results shows that the NI MHD turbulence transport equations can describe the evolution of turbulence throughout the heliosphere.

Acknowledgments

We acknowledge the partial support of a Parker Solar Probe contract SV4-84017, an NSF EPSCoR RII-Track-1 cooperative agreement OIA-1655280, and NASA awards 80NSSC20K1783 and 80NSSC21K1319, and NASA Heliospheric Shield 80NSSC22M0164, and the SWAP instrument effort on the New Horizons project (M99023MJM; PU-A WD1006357), with support from NASA's New Frontiers Program and the IMAP mission as a part of NASA's Solar Terrestrial Probes (STP) mission line (80GSFC19C0027). A.P. acknowledges the partial support by the Czech Grant Agency under contract (23-06401S).

Appendix Closure Relations

The closure A10 is written as (Zank et al. 2012a)

$$F_{i}\left\langle z_{j}^{+} \frac{\partial z_{j}^{-}}{\partial x_{i}} - z_{j}^{-} \frac{\partial z_{j}^{+}}{\partial x_{i}} \right\rangle$$

$$\simeq F_{i}\left[\langle z_{j}^{+2} \rangle^{1/2} \frac{\partial}{\partial x_{i}} \langle z_{j}^{-2} \rangle^{1/2} - \langle z_{j}^{-2} \rangle^{1/2} \frac{\partial}{\partial x_{i}} \langle z_{j}^{+2} \rangle^{1/2} \right];$$

$$= F_{i}\left[\frac{1}{2} \left(\frac{\langle z_{j}^{+2} \rangle}{\langle z_{j}^{-2} \rangle} \right)^{1/2} \frac{\partial}{\partial x_{i}} \langle z_{j}^{-2} \rangle - \frac{1}{2} \left(\frac{\langle z_{j}^{-2} \rangle}{\langle z_{j}^{+2} \rangle} \right)^{1/2} \frac{\partial}{\partial x_{i}} \langle z_{j}^{+2} \rangle \right];$$

$$= \frac{1}{2} \frac{1}{\sqrt{\langle z_{j}^{+2} \rangle \langle z_{j}^{-2} \rangle}} \left[\left\langle z_{j}^{+2} \rangle F_{i} \frac{\partial}{\partial x_{i}} \langle z_{j}^{-2} \rangle - \langle z_{j}^{-2} \rangle F_{i} \frac{\partial}{\partial x_{i}} \langle z_{j}^{+2} \rangle \right]$$

$$= \frac{1}{2} \frac{1}{\sqrt{\langle z^{+2} \rangle \langle z^{-2} \rangle}} (\langle z^{+2} \rangle F \cdot \nabla \langle z^{-2} \rangle - \langle z^{-2} \rangle F \cdot \nabla \langle z^{+2} \rangle).$$
(35)

The closure C10 is written as (Zank et al. 2012a)

$$\int_{o}^{\infty} \langle (V_{A} \cdot \nabla z^{-'}) \cdot z^{+} + (V_{A} \cdot \nabla z^{-}) \cdot z^{+'} \\
-(V_{A} \cdot \nabla z^{+}) \cdot z^{-'} - (V_{A} \cdot \nabla z^{+'}) \cdot z^{-} \rangle dr \\
\simeq \left(\frac{L^{+}}{L^{-}}\right)^{1/2} V_{A} \cdot \nabla L^{-} - \left(\frac{L^{-}}{L^{+}}\right)^{1/2} V_{A} \cdot \nabla L^{+}.$$
(36)

ORCID iDs

Laxman Adhikari https://orcid.org/0000-0003-1549-5256 Gary P. Zank https://orcid.org/0000-0002-4642-6192 Bingbing Wang https://orcid.org/0000-0002-6000-1262 Lingling Zhao https://orcid.org/0000-0002-4299-0490 Daniele Telloni https://orcid.org/0000-0002-6710-8142 Merav Opher https://orcid.org/0000-0002-8767-8273 Bishwas Shrestha https://orcid.org/0000-0002-5247-4107 David J. McComas https://orcid.org/0000-0001-6160-1158

References

```
Adhikari, L., Zank, G. P., Bruno, R., et al. 2015, ApJ, 805, 63
Adhikari, L., Zank, G. P., Hu, Q., & Dosch, A. 2014, ApJ, 793, 52
Adhikari, L., Zank, G. P., Hunana, P., et al. 2017a, ApJ, 841, 85
Adhikari, L., Zank, G. P., Telloni, D., et al. 2017b, ApJ, 851, 117
Adhikari, L., Zank, G. P., Telloni, D., & Zhao, L. L. 2022a, ApJL, 937, L29
Adhikari, L., Zank, G. P., & Zhao, L. 2021a, Fluid, 6, 368
Adhikari, L., Zank, G. P., & Zhao, L. L. 2020a, ApJ, 901, 14
Adhikari, L., Zank, G. P., Zhao, L. L., et al. 2020b, ApJS, 246, 38
Adhikari, L., Zank, G. P., Zhao, L. L., Nakanotani, M., & Tasnim, S. 2021b, A&A, 650, A16
Adhikari, L., Zank, G. P., Zhao, L. L., & Telloni, D. 2022b, ApJ, 938, 120
Adhikari, L., Zank, G. P., Zhao, L. L., & Telloni, D. 2022c, ApJ, 933, 56
```

```
Aggarwal, P., Taylor, D. K., Smith, C. W., et al. 2016, ApJ, 822, 94
Armstrong, J. W., Cordes, J. M., & Rickett, B. J. 1981, Natur, 291, 561
Armstrong, J. W., Rickett, B. J., & Spangler, S. R. 1995, ApJ, 443, 209
Axford, W. I. 1972, in Solar Wind, ed. C. P. Sonett, P. J. Coleman, &
  J. M. Wilcox, 308 (Washington, D.C.: NASA), 609
Batchelor, G. K. 1953, The Theory of Homogeneous Turbulence (Cambridge:
  Cambridge Univ. Press)
Bhattacharjee, A., Ng, C. S., & Spangler, S. R. 1998, ApJ, 494, 409
Breech, B., Matthaeus, W. H., Cranmer, S. R., Kasper, J. C., & Oughton, S.
  2009, JGRA, 114, A09103
Breech, B., Matthaeus, W. H., Minnie, J., et al. 2008, JGRA, 113, 8105
Burlaga, L. F., Ness, N. F., & Richardson, J. D. 2003, JGRA, 108, 8028
Cannon, B. E., Smith, C. W., Isenberg, P. A., et al. 2014, ApJ, 784, 150
Chhiber, R. 2022, ApJ, 939, 33
Cranmer, S. R., Matthaeus, W. H., Breech, B. A., & Kasper, J. C. 2009, ApJ,
  702, 1604
Di Matteo, S., Viall, N. M., Kepko, L., et al. 2019, JGRA, 124, 837
Dosch, A., Adhikari, L., & Zank, G. P. 2013, in AIP Conf. Ser. 1539, SOLAR
   WIND 13 (Melville, NY: AIP), 155
Elliott, H. A., McComas, D. J., Zirnstein, E. J., et al. 2019, ApJ, 885, 156
Fisher, M. K., Argall, M. R., Joyce, C. J., et al. 2016, ApJ, 830, 47
Holzer, T. E. 1972, JGR, 77, 5407
Hunana, P., & Zank, G. P. 2010, ApJ, 718, 148
Hunana, P., Zank, G. P., Heerikhuisen, J., & Shaikh, D. 2008, JGRA, 113, A11105
Hunana, P., Zank, G. P., & Shaikh, D. 2006, PhRvE, 74, 026302
Isenberg, P. A., Vasquez, B. J., & Smith, C. W. 2023, ApJ, 944, 84
Kallenbach, R., Geiss, J., Gloeckler, G., & von Steiger, R. 2000, Ap&SS, 274, 97
Kepko, L., Viall, N. M., & Wolfinger, K. 2020, JGRA, 125, e28037
Klainerman, S., & Majda, A. 1981, CPAM, 34, 481
Klainerman, S., & Majda, A. 1982, CPAM, 35, 629
Korolkov, S. D., & Izmodenov, V. V. 2022, A&A, 667, L5
Larrodera, C., & Cid, C. 2020, A&A, 635, A44
Lee, M. A. 1995, in Int. Solar Wind 8 Conf. (Dana Point, CA: CalTech), 109
Marsch, E., & Tu, C.-Y. 1989, JPIPh, 41, 479
Matthaeus, W. H., Oughton, S., Pontius, D. H., Jr., & Zhou, Y. 1994, JGR, 99,
Matthaeus, W. H., Zank, G. P., Oughton, S., Mullan, D. J., & Dmitruk, P.
  1999a, ApJL, 523, L93
Matthaeus, W. H., Zank, G. P., Smith, C. W., & Oughton, S. 1999b, PhRvL,
  82, 3444
McComas, D., Allegrini, F., Bagenal, F., et al. 2008, SSRv, 140, 261
McComas, D. J., Shrestha, B. L., Swaczyna, P., et al. 2022, ApJ, 934, 147
McComas, D. J., Swaczyna, P., Szalay, J. R., et al. 2021, ApJS, 254, 19
Montgomery, D., Brown, M. R., & Matthaeus, W. H. 1987, JGR, 92, 282
Nakanotani, M., Zank, G. P., Adhikari, L., et al. 2020, ApJL, 901, L23
Oughton, S., Matthaeus, W. H., Smith, C. W., Breech, B., & Isenberg, P. A.
  2011, JGRA, 116, 8105
Pine, Z. B., Smith, C. W., Hollick, S. J., et al. 2020, ApJ, 900, 94
Richardson, J. D., Paularena, K. I., Lazarus, A. J., & Belcher, J. W. 1995,
   GeoRL, 22, 1469
Richardson, J. D., & Wang, C. 2003, in AIP Conf. Ser. 679, SOLAR WIND
  TEN, ed. M. Velli (Melville, NY: AIP), 71
Rucinski, D., & Bzowski, M. 1995, A&A, 296, 248
Smith, C. W., Isenberg, P. A., Matthaeus, W. H., & Richardson, J. D. 2006,
  ApJ, 638, 508
Swaczyna, P., McComas, D. J., Zirnstein, E. J., et al. 2020, ApJ, 903, 48
Telloni, D., Adhikari, L., Zank, G. P., et al. 2022a, ApJL, 938, L8
Telloni, D., Adhikari, L., Zank, G. P., et al. 2022b, ApJ, 929, 98
Usmanov, A. V., Goldstein, M. L., & Matthaeus, W. H. 2012, ApJ, 754, 40
Usmanov, A. V., Matthaeus, W. H., Goldstein, M. L., & Chhiber, R. 2018,
   ApJ, 865, 25
Vasyliunas, V. M., & Siscoe, G. L. 1976, JGR, 81, 1247
Verdini, A., Velli, M., Matthaeus, W. H., Oughton, S., & Dmitruk, P. 2010,
Wang, B. B., Zank, G. P., Adhikari, L., & Zhao, L. L. 2022, ApJ, 928, 176
Wang, C., Richardson, J. D., & Gosling, J. T. 2000, GeoRL, 27, 2429
Weber, E. J., & Davis, L., Jr. 1967, ApJ, 148, 217
Williams, L. L., & Zank, G. P. 1994, JGR, 99, 19229
Zank, G. P. 1999, SSRv, 89, 413
Zank, G. P. 2014, Transport Processes in Space Physics and Astrophysics
   (Berlin: Springer)
Zank, G. P., Adhikari, L., Hunana, P., et al. 2017, ApJ, 835, 147
Zank, G. P., Adhikari, L., Hunana, P., et al. 2018a, ApJ, 854, 32
Zank, G. P., Adhikari, L., Zhao, L. L., et al. 2018b, ApJ, 869, 23
Zank, G. P., Dosch, A., Hunana, P., et al. 2012a, ApJ, 745, 35
Zank, G. P., Hunana, P., Mostafavi, P., & Goldstein, M. L. 2014, ApJ, 797, 87
```

```
Zank, G. P., Jetha, N., Hu, Q., & Hunana, P. 2012b, ApJ, 756, 21
Zank, G. P., & Matthaeus, W. H. 1991, PhFIA, 69, 3
Zank, G. P., & Matthaeus, W. H. 1992a, JPIPh, 48, 85
Zank, G. P., & Matthaeus, W. H. 1992b, JGR, 97, 17189
Zank, G. P., & Matthaeus, W. H. 1993, PhFI, 5, 257
Zank, G. P., Matthaeus, W. H., & Klein, L. W. 1990, GeoRL, 17, 1239
Zank, G. P., Matthaeus, W. H., & Smith, C. W. 1996, JGR, 101, 17093
Zank, G. P., Nakanotani, M., Zhao, L. L., Adhikari, L., & Telloni, D. 2020, ApJ, 900, 115
```

```
Zank, G. P., Zhao, L. L., Adhikari, L., et al. 2021, PhPl, 28, 080501
Zank, G. P., Zhao, L. L., Adhikari, L., et al. 2022, ApJL, 926, L16
Zhao, L. L., Adhikari, L., Zank, G. P., Hu, Q., & Feng, X. S. 2017, ApJ, 849, 88
Zhao, L.-L., Adhikari, L., Zank, G. P., Hu, Q., & Feng, X. S. 2018, ApJ, 856, 94
Zhao, L. L., Zank, G. P., & Adhikari, L. 2019, ApJ, 879, 32
Zhou, Y., & Matthaeus, W. H. 1990a, JGR, 95, 14881
Zhou, Y., & Matthaeus, W. H. 1990b, JGR, 95, 14863
```